



Holey Ni-Cu phosphide nanosheets as a highly efficient and stable electrocatalyst for hydrogen evolution

Sijun Chu^{a,1}, Wei Chen^{b,1}, Guangliang Chen^{a,*}, Jun Huang^{b,*}, Rui Zhang^a, Changsheng Song^{a,*}, Xingquan Wang^b, Chaorong Li^a, Kostya (Ken) Ostrikov^c

^a Key Laboratory of Advanced Textile Materials and Manufacturing Technology and Engineering Research Center for Eco-Dyeing & Finishing of Textiles, Ministry of Education, Zhejiang Sci-Tech University, Hangzhou, 310018, China

^b College of Physics and Electronic Information, Gannan Normal University, Ganzhou, Jiangxi, 341000, China

^c School of Chemistry, Physics and Mechanical Engineering, Queensland University of Technology, Brisbane, QLD, 4000, Australia

ARTICLE INFO

Keywords:

Heteroatom doping
Electrocatalyst
Metal phosphide
HER
DFT

ABSTRACT

Hydrogen, generated by electrocatalytic process, is one of the most promising sources of green and sustainable energy. Herein, we report a novel electrocatalyst for hydrogen evolution reaction (HER) fabricated by doping Ni foam (NF) supported Ni₂P nanosheets with Cu atoms. The Cu atoms effectively tune the structure and physicochemical properties of Ni₂P, leading to the lower HER free energy, improved electrical conductivity, and high exposure of surface active sites. The optimized Ni_{1.8}Cu_{0.2}-P displays an excellent catalytic performance and stability, which is demonstrated by the low overpotentials of 78 (Tafel slope: 70 mV dec⁻¹) and 245 mV to reach a current density of 10 and 100 mA cm⁻² for the HER in 1.0 M KOH. The high electrocatalytic activity of Ni_{1.8}Cu_{0.2}-P is attributed to the increased Fermi level and the exposed active crystal plane (201). The H₂ amount produced with a current density of 10 mA cm⁻² is about 1.91 mmol h⁻¹ cm⁻², which is the highest value among the reported non-precious metal catalysts.

1. Introduction

The ever escalating energy crisis impedes social and economic growth of human society. Because of the strong need to change this adverse trend, search for new green and sustainable energy sources is of paramount importance for both research and industry sectors [1–4]. Hydrogen gas is considered as the most promising renewable energy, due to its advantages, such as the highest energy density compared to other fuels, no harmful gases emissions, and good compatibility with advanced energy technologies [5–9]. Nowadays, the fuels conversion [10] and water splitting [11,12] are viewed as the two primary protocols for producing hydrogen. Recently, the electrolysis of water has been particularly important for advancing green and sustainable energy fields [13–17], because it is a highly-effective and energy-efficient way to transform electricity into clean energy that can be stored in chemical bonds of hydrogen molecules. However, search for novel electrocatalysts is on the agenda with the aim to decrease the energy input characterized by the overpotential values and to accelerate the reaction kinetics of water electrolysis. The noble metals such as Pt-group based metals are still the most robust electrocatalysts for HER, even though

many state-of-the-art catalysts with high electrocatalytic activity have been reported. Nevertheless, the scarcity of these noble catalysts and high cost restrict their wide practical applications [18–20]. Thus, exploring non-noble and high-efficiency catalysts, as alternatives based on Pt materials for HER, is critical to enable commercial applications of water electrolysis for energy conversion, storage, and transportation.

To overcome the problems mentioned above, over the past few decades, substantial efforts for exploring high-efficiency precious metals substitutes have been made to develop non-precious metal electrocatalysts with excellent electrocatalytic activity in HER process, like carbon materials [21], perovskites [22], transition-metal sulfides [23–25], oxides [26], nitrides [27], phosphides [28], and so on. Among these catalysts, transition metal phosphides (TMPs) are highly-efficient, robust, and inexpensive, and have attracted a great deal of attention [29–35]. The excellent catalytic performance of TMPs is attributed to isolated metal and non-metal atoms which act as selective hydride-acceptor and proton-acceptor sites on the transition metal phosphides surface [36]. For example, a wide class of TMPs, such as Ni₂P [37,38], CoP [39–41], MoP [42,43], FeP [44,45], have been reported, and they showed a good electrocatalytic performance for HER in alkaline

* Corresponding authors.

E-mail addresses: glchen@zstu.edu.cn (G. Chen), junhuang66@163.com (J. Huang), cssong@zstu.edu.cn (C. Song).

¹ These authors contributed equally to this work.

solution. In addition, ongoing research proved the key factors that determine the HER kinetics: (i) Nanoscale morphology and surface area of the catalysts (e.g., determined by nanostructures or nanotextures); (ii) Catalyst stability (e.g., degradation rates) in harsh (e.g., strong acid or base) electrochemical environments; (iii) Dynamic formation and stability of amorphous or crystalline phases on the surface; (iv) Composite catalysts with the optimum composition allow faster mass transfer, provide more catalytically active sites, and lead to faster hydrogen production [46–49].

Despite exceptional promise, applications of Ni_2P as hydrogen evolution reaction (HER) electrocatalyst is hindered mostly due to the (i) still higher overpotential compared to noble metal based catalysts, (ii) essentially unclear cause-and-effect relationship between the exposed crystal planes and the HER activity; (iii) limited stability of the catalyst especially in harsh environments. Based on the fact that copper phosphide exhibits super electrocatalytic stability for overall water splitting [50], and we anticipate that heteroatom doping of Ni_2P nanosheets with Cu may improve the electrocatalytic stability and activity of the catalyst. However, any experimental confirmation of this highly-promising possibility is lacking.

This work fills this knowledge gap by developing a novel HER catalyst based on three-dimensional (3D) Ni foam (NF)-supported Ni_2P nanosheets doped with different amount of Cu; this material is denoted $\text{Ni}_{2-x}\text{Cu}_x\text{-P/NF}$ with x ranging from 0 to 0.6. The nanosized materials were achieved via a two-step synthesis process consisting of the synthesis of NiCu layered double hydroxide (NiCu LDH) nanosheets arrays on nickel foam, followed by phosphating to get, and the whole process is summarized in Fig. 1. The Cu atoms tune the electric structure of Ni_2P , and the fabricated $\text{Ni}_{1.8}\text{Cu}_{0.2}\text{-P/NF}$ shows a superior HER performance in alkaline medium. As a result, an overpotential of 78 mV (HER) to deliver 10 mA cm^{-2} is achieved. Importantly, the demonstrated hydrogen generation efficiency (1.91 $\text{mmol h}^{-1} \text{cm}^{-2}$) surpasses most of the reported state-of-the-art electrocatalysts.

2. Experimental section

2.1. Chemical Reagents

Ni foam (NF) (thickness: 1 mm) was provided by Kunshan Jiayisheng Electronics Co., Ltd. Acetone (CH_3COCH_3 , $\geq 99.5\%$), ethyl alcohol ($\text{CH}_3\text{CH}_2\text{OH}$, 99.7%), Pt/C (20 wt.%), Nafion (5 wt. %), hydrochloric acid (HCl), potassium hydroxide (KOH, 85.0%), sodium hypophosphite (NaH_2PO_2 , 99.0%), urea ($\text{CO}(\text{NH}_2)_2$, 99.0%),

ammonium fluoride (NH_4F , 96.0%), nickel nitrate hexahydrate ($\text{Ni}(\text{NO}_3)_2 \cdot 6\text{H}_2\text{O}$, 98.0%), copper nitrate hemi (pentahydrate) ($\text{Cu}(\text{NO}_3)_2 \cdot 3\text{H}_2\text{O}$, 99.0%) were purchased from the Hangzhou MinLing Chemical Instrument Co., Ltd. During the sample manufacturing process, the deionized water was used, and each chemical was analytically grade and required no further purification.

2.2. Synthesis of $\text{Ni}_{2-x}\text{Cu}_x\text{-P}$ nanosheets on Nickel foam (NF)

2.2.1. Synthesis of NiCu LDH/NF

Firstly, a piece of NF (20 mm \times 30 mm) was carefully rinsed with acetone (20 ml) in an ultrasound bath for 10 min, and followed with the hydrochloric acid (3 M, 20 ml) for a cleaning time of 10 min. Then, the deionized water and absolute ethanol were successively used to clean the surface, and the cleaned NF was put in a 50 °C oven until it was dry enough [7]. The NiCu-LDH/NF material was prepared by means of hydrothermal process. The precursors of urea (8 mmol), NH_4F (6 mmol), $\text{Ni}(\text{NO}_3)_2 \cdot 6\text{H}_2\text{O}$ and $\text{Cu}(\text{NO}_3)_2 \cdot 3\text{H}_2\text{O}$ with different mole ratios of Ni/Cu (2/0, 1.8/0.2, 1.6/0.4, 1.4/0.6, 0/2 at an invariable total metal ion concentration of 2 mmol) were magnetically dissolved in 30 mL of deionized water. The mixed solution and the Ni foam were moved into a 50 mL Teflon-line stainless-steel autoclave, and the sealed reactor maintained at 120 °C for 6 h in a drying oven. The as-fabricated material was respectively cleaned with deionized water and ethanol for three times. At last, the obtained sample (NiCu LDH/NF) was dried in a vacuum oven at 50 °C for 12 h.

2.2.2. Phosphatization of NiCu LDH/NF

The obtained NiCu LDH/NF samples were placed at the center of the tube furnace, and a ceramic boat loaded with 4.7 mmol NaH_2PO_2 powder was placed at upstream side of the NiCu LDH/NF. The samples were heated to 350 °C with a heating speed of 5 °C min^{-1} in Ar flow atmosphere for 1 h to convert the NiCu LDH/NF to $\text{Ni}_{2-x}\text{Cu}_x\text{-P/NF}$. The product was collected after cooling down to room temperature under the protection gas of Ar, and the materials were rinsed with deionized water until the water was neutral.

2.3. Microstructure Characterization

The fabricated samples were characterized using a JSM-6700 F field-emission scanning electron microscopy (FE-SEM, JEOL, Japan) with 3 kV electron beam accelerating voltage, and a transmission electron microscopy (TEM) system (Model JSM-2100, JEOL, Japan).

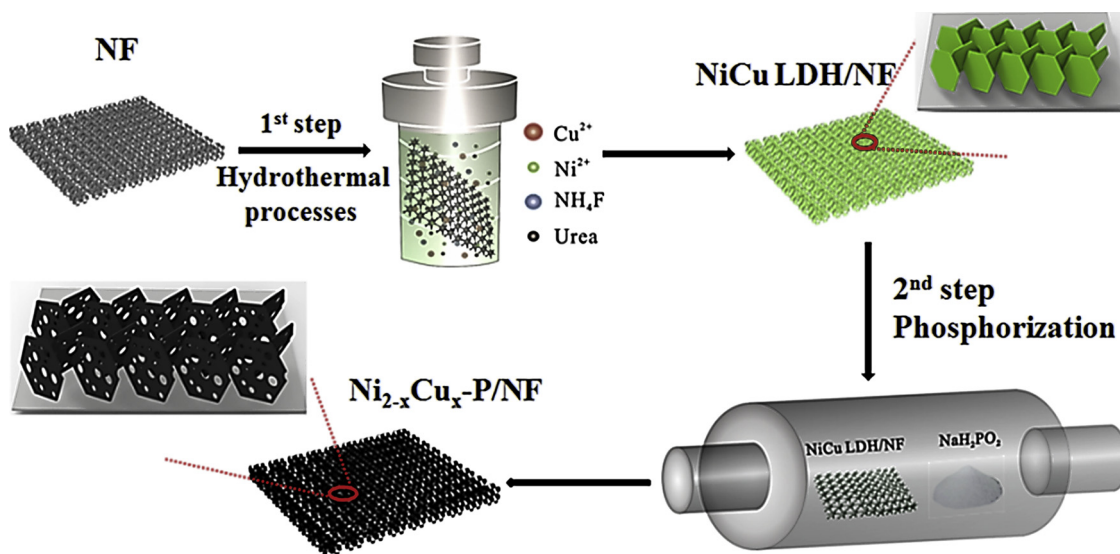


Fig. 1. Process steps in the synthesis of high-performance $\text{Ni}_{2-x}\text{Cu}_x\text{-P}$ electrocatalysts.

Spherical aberration corrected (Cscorrected) high angle annular dark field scanning transmission electron-microscopy (HAADF-STEM) and energy-dispersive X-ray (EDX) mapping images were obtained with an FEI Titan G2 microscope equipped with a Super-X detector, operating at 300 kV. The X-ray diffractometer (XRD, Thermo Fisher Scientific, USA) was used to obtain the X-ray diffraction (XRD) patterns of nanocomposite using a Cu K α radiation source at 35 kV, and an X-ray photoelectron spectrometer (XPS) (Kratos Axis Ultra DLD) with an Al K α source (1486.6 eV) was used to measure the surface chemical composition of as-prepared samples. The profiles of NiCu LDH and Ni_{2-x}Cu_x-P nanosheets were investigated through an atomic force microscopy (AFM, Model XE-100E, Korea). The Raman spectra were measured with a micro Raman spectrometer (Renishaw Via), and the excitation source is a DPSS laser of 532 nm. It should be noted that the mass of Ni_{2-x}Cu_x-P formed on the NF was recorded by a precision balance (delta: 0.001 mg).

2.4. Electrochemical measurements

Electrochemical measurements in different electrolytes were performed by a computer-controlled electrochemical workstation (Model CHI750E, Shanghai Chenhua Instrument Co., Ltd.) with a three-electrode cell at an ambient condition. The resulting specimen (0.5 cm \times 0.5 cm) acted as the working electrode, and the carbon rod was used as the counter electrode while the Hg/HgO electrode acted as the reference electrode. All the potentials reported herein were referred to the reversible hydrogen electrode (RHE) in accordance with the following equation: $E(\text{RHE}) = E(\text{Hg/HgO}) + 0.095 + 0.059 \text{ pH}$ [51,52]. The electrocatalytic activity of sample was measured by using Linear-sweep voltammetry (LSV) at a scan rate of 2 mV s^{-1} in 1 M KOH, and iR corrected. The Nyquist plots were obtained by Electrochemical impedance spectroscopy (EIS) measured in the frequency range from 100 KHz to 1 Hz under 1 M KOH solution. For long-term cyclic voltammetry (CV) test of HER, the Ni_{1.8}Cu_{0.2}-P/NF electrodes was examined at a scan rate of 100 mV s^{-1} for 10000 cycles at first with a current density of -10 mA cm^{-2} , and the ultimate CV polarization curves were recorded at a scanning speed of 1 mV s^{-1} again. It should be noted that measurement of noble-metal electrode (Pt/C), and the calculations of electrochemical double layer capacitances (C_{dl}) and turn over frequencies (TOF) of the resulting catalysts followed with similar methods as the reported references [50,53–56]. Meanwhile, the active sites of fabricated catalysts were estimated by the N₂ adsorption-desorption isotherm (3H-2000PS1 static volume method, Beishide Instrument Tech. Co. LTD.).

3. Results and discussion

3.1. Morphological and structural characterizations

For the fabrication of nanosized Ni_{2-x}Cu_x-P architecture, the NiCu LDH nanosheets were firstly grown on the commercial 3D porous nickel foam. As shown in Fig. 2a, many NiCu LDH nanosheets and a few of microflowers (Fig. 2a: inset) assembled with NiCu LDH nanosheets were formed on the NF frame. With a high magnification (Fig. 2b), it can be noticed that the cross-linked NiCu LDH nanosheets formed on the NF surface, which is very useful for enhancing the electrocatalytic activity and stability in HER process. Meanwhile, the thickness of NiCu LDH nanosheet was about 16 nm, as shown in Fig. S1a, and the thin NiCu LDH can expose a large surface area for electrocatalytic reaction. Subsequently, the resulting NiCu LDH on the NF surface was subjected to phosphidation to get the 3D hierarchical Ni_{1.8}Cu_{0.2}-P/NF, and the nanosheet thickness was only 12 nm (Fig. S1b). Moreover, as shown in Fig. 2c, many nanoholes were formed on the nanosheets, which will play an important role in the HER process as they increase electron transfer rates and the contact area with the electrolyte [56].

Meanwhile, the crystal structure of Ni_{1.8}Cu_{0.2}-P/NF was measured by the XRD spectroscopy. Compared with the NiCu LDH/NF (blue line

in Fig. 2d), new peaks occurred (black line in Fig. 2d) after a phosphatizing method, such as $2\theta = 40.7^\circ$, 44.6° , 47.4° , and 54.2° which correspond to (111), (201), (210) and (300) planes of Ni₂P, respectively (JCPDS PDF 74-1385); the double angles $2\theta = 35.5^\circ$, 44.0° , 45.6° , 57.8° and 65.3° correspond to (102), (110), (013), (022) and (203) crystal planes of Cu₃P, respectively (JCPDS PDF 72-0807) [50]. These results suggest that the NiCu LDH/NF was transformed to the crystalline form Ni_{1.8}Cu_{0.2}-P/NF. Fig. 2e shows the elemental mapping of Ni, Cu, P and O atoms on the surface of Ni_{1.8}Cu_{0.2}-P/NF nanocomposite, indicating a homogeneous distribution of these elements on the resulting nanosheets. It should be noted that the O element may be originated from the oxidized layer of Ni_{1.8}Cu_{0.2}-P/NF catalyst.

The crystal and morphology structure of Ni_{1.8}Cu_{0.2}-P was further detected by TEM. As the Fig. 3a shows, the hydrangea-like microspheres that form on the NF surface represent a stack of many cross-linked Ni_{1.8}Cu_{0.2}-P nanosheets. This feature will be very useful for increasing the electrocatalytic stability in the following HER process. Due to a higher magnification (Fig. 3b), it was observed that many nanoholes occurred on the nanosheet of Ni_{1.8}Cu_{0.2}-P, and the porous structure facilitate the electron transfer, the H⁺ adsorption/desorption, and enable an intimate contact with electrolyte, which is considered beneficial for increasing the electrocatalytic activity and hence the amount of hydrogen gas produced [54,55]. Fig. 3c exhibits the high-resolution TEM of Ni_{1.8}Cu_{0.2}-P, and the mixing phase with interplanar spacing of 0.246 and 0.251 nm, corresponding to the (201) planes of Ni₂P and (013) planes of Cu₃P, respectively. Meanwhile, the occurrences of these crystal facets were also identified through the selected area electron diffraction (SAED) patterns (Fig. 3d), which is consistent with the XRD results. Furthermore, the crystal characteristics of Ni_{1.8}Cu_{0.2}-P indicate that the Cu atoms were successfully doped into the Ni₂P cell. This doping can be used to tune the Fermi level of Ni₂P effectively, thus positively contributing to the enhancement of HER activity [53]. The elemental mapping of Ni_{1.8}Cu_{0.2}-P is shown in Fig. 3e, and it indicates that a homogeneous distribution of various elements including Ni, Cu, P and O in the Ni_{1.8}Cu_{0.2}-P nanosheets, which are consistent with the EDX microanalysis of SEM. It should be noted that O atom mainly come from the oxide layer of Ni_{1.8}Cu_{0.2}-P or the NiCu LDH without phosphatized.

We further performed the XPS measurements to probe the surface composition of Ni_{1.8}Cu_{0.2}-P. As shown in Fig. 4a, the high-resolution Ni 2p can be deconvoluted into two peaks centered at binding energies of 856.2 eV (Ni 2p_{3/2}) and 874.8 eV (Ni 2p_{1/2}), assignable to Ni²⁺ in Ni₂P [51,57]. The peaks at 861.8 and 879.5 eV are the satellites of Ni-PO_x [54,58]. In addition, the peaks at 853.0 and 870.4 eV suggest the existence of Ni ^{$\delta+$} ($0 < \delta < 2$) in Ni₂P [38]. It should be noted that the binding energy of 853.0 eV is very close to the peak of metallic Ni (852.6 eV), indicating the existence of Ni substrate. Fig. 4b presents the high-resolution XPS spectrum of Cu 2p, which is deconvoluted into two peaks at 932.2 and 952.2 eV respectively, corresponding to the Cu 2p_{3/2} and Cu 2p_{1/2} in copper phosphide [50]. Similarly, the P 2p segment of converted Ni_{1.8}Cu_{0.2}-P (Fig. 4c) has two peak binding energies at 129.5 and 134.4 eV. The former can be assigned to reduced P 2p_{3/2} in the form of metal phosphides, and the other peak at 134.4 eV reflected the oxidized phosphorus species (P 2p_{1/2}) [38]. The deconvoluted peak at 130.2 eV is near to that of element P (130 eV). Moreover, fractional negative charge (P ^{$\delta-$}) helps P atoms capture positively charges protons as one of the fundamental reaction steps during the electrocatalytic HER process [54]. It should be noted that the O element (Table S1) was also detected in the Ni_{1.8}Cu_{0.2}-P, and the O 1s band was deconvoluted into two peaks. The peak at 531.9 eV may come from the phosphate generated by the surface oxidation of Ni_{1.8}Cu_{0.2}-P or the OH⁻ species contained in the NiCu LDH, while the peak with a higher binding energy (at 533.4 eV) was allocated to chemically adsorbed oxygen.

3.2. Hydrogen evolution reaction performance

The HER performances of the original NF, NiCu LDH/NF, Ni_{1.8}Cu_{0.2}-

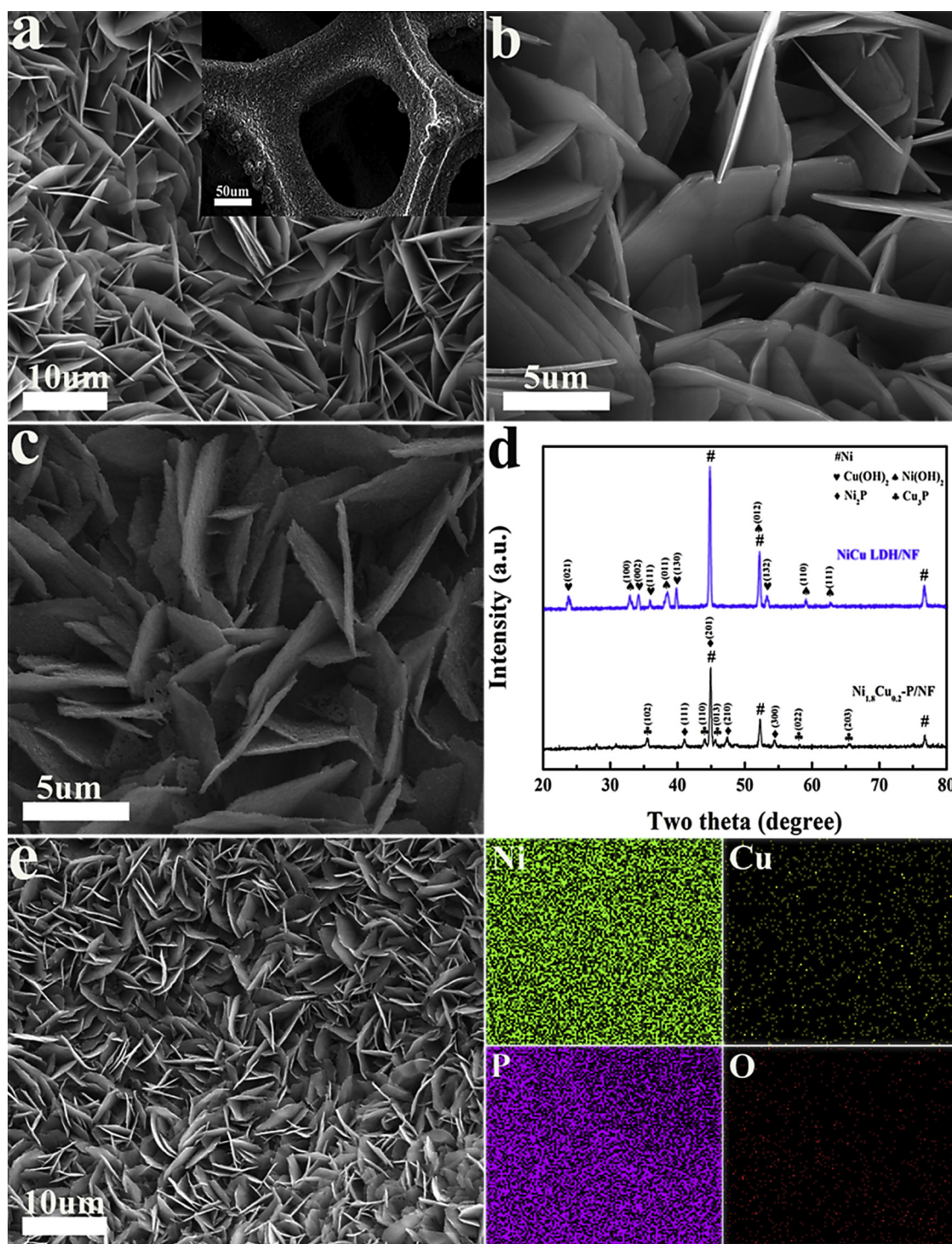


Fig. 2. SEM images of NF frame coated by NiCu LDH obtained with a low (a) and high (b) resolution; the inset in (a) is the frame structure of NF coated with NiCu LDH, (c) High-magnification SEM images of Ni_{1.8}Cu_{0.2}-P/NF, (d) XRD patterns of NiCu LDH/NF and Ni_{1.8}Cu_{0.2}-P/NF, (e) SEM profile of Ni_{1.8}Cu_{0.2}-P/NF and the corresponding elemental mapping of Ni_{1.8}Cu_{0.2}-P/NF.

P/NF, commercial Pt/C coated on the NF were measured in 1 M KOH aqueous electrolyte by means of a standard three-electrode system. The comparison in Fig. 5a shows that the Ni_{1.8}Cu_{0.2}-P/NF displays a much higher electrocatalytic performance than NF and NiCu LDH/NF. In particular, a current density of 10 mA cm⁻² can be obtained at overpotential as low as 78 mV on Ni_{1.8}Cu_{0.2}-P/NF, which is far lower than NF (172 mV) and NiCu LDH/NF (136 mV), even lower than those catalysts with different Ni/Cu ratios (see Fig. S2a) that sustain the same current density (10 mA cm⁻²), such as Ni₂P (103 mV), Cu₃P (117 mV),

Ni_{1.6}Cu_{0.4}-P/NF (86 mV) and Ni_{1.4}Cu_{0.6}-P/NF (101 mV). In the meantime, the high electrocatalytic performance of the fabricated Ni_{1.8}Cu_{0.2}-P/NF is also confirmed through the calculated H₂ turn over frequencies (TOFs), and the TOF of Ni_{1.8}Cu_{0.2}-P/NF is clearly higher than that of NiCu LDH/NF (see Table S2). Although the HER efficiency of Ni_{1.8}Cu_{0.2}-P/NF is still lower compared to commercial Pt-C/NF (52 mV), the overpotential at 10 mA cm⁻² is very competitive to the newly reported catalysts, including NF-Ni₃S₂/NF (135 mV) [59], P-Co₃O₄ (120 mV) [60], Cu@NiFe LDH (116 mV) [56], FeCo@NC (150 mV) [61], and

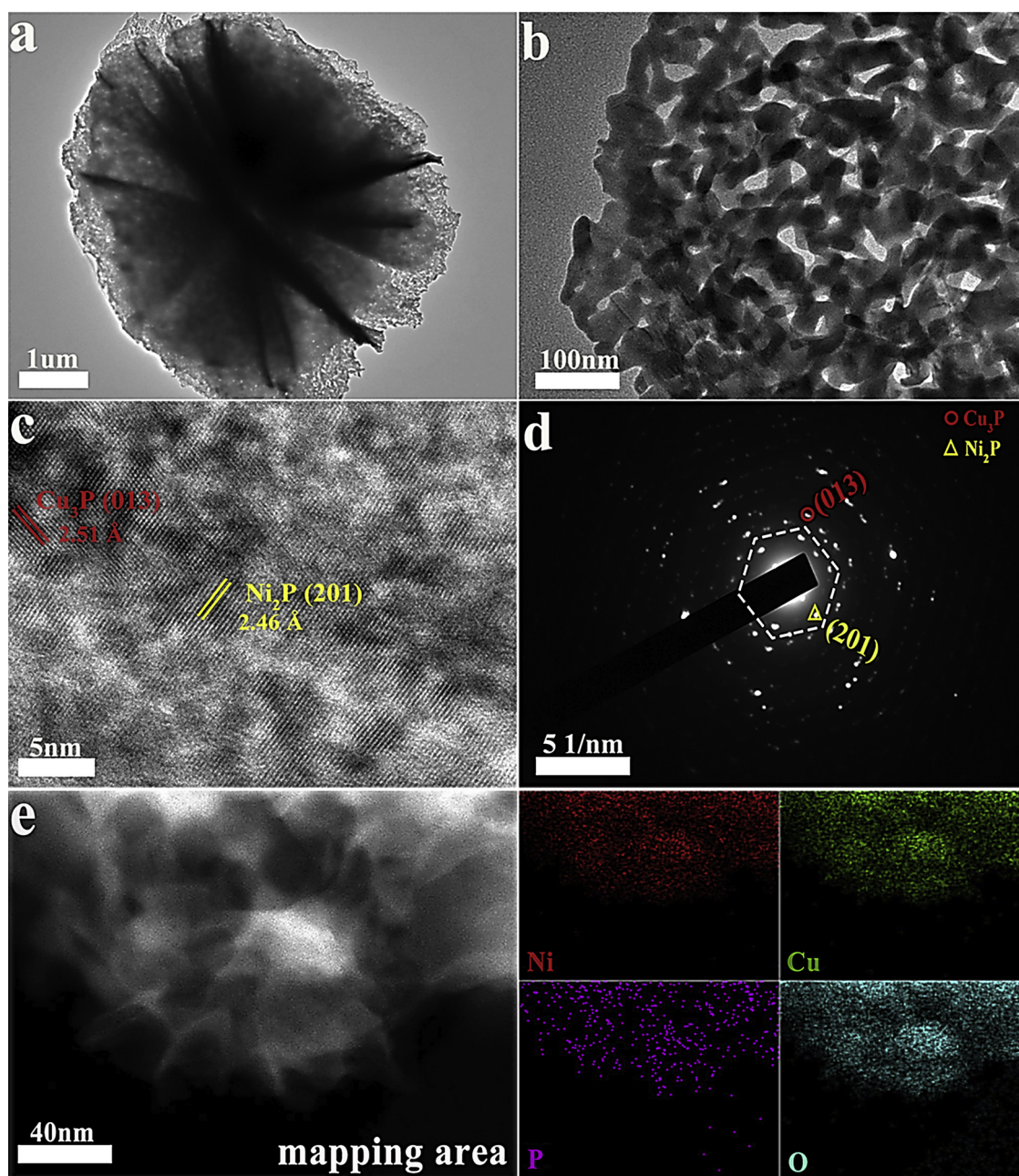


Fig. 3. TEM of $\text{Ni}_{1.8}\text{Cu}_{0.2}\text{-P/NF}$. (a) Low-resolution of $\text{Ni}_{1.8}\text{Cu}_{0.2}\text{-P}$ microflower on the NF frame, (b) A single $\text{Ni}_{1.8}\text{Cu}_{0.2}\text{-P}$ nanosheet, (c) High-resolution of $\text{Ni}_{1.8}\text{Cu}_{0.2}\text{-P}$, (d) SAED pattern obtained from the $\text{Ni}_{1.8}\text{Cu}_{0.2}\text{-P}$ nanosheet, and (e) HAADF-STEM image of $\text{Ni}_{1.8}\text{Cu}_{0.2}\text{-P}$ and STEM-EDX elemental mapping for Ni, Cu, P and O, respectively.

many other reported non-noble metal based electrocatalysts (see Table S3).

Fig. 5b shows the Tafel plots of the catalysts derived from the LSV curves in Fig. 5a, and the Tafel slope of $\text{Ni}_{1.8}\text{Cu}_{0.2}\text{-P/NF}$ is calculated to be 70 mV dec^{-1} , which is far smaller than those of NiCu LDH/NF (154 mV dec^{-1}), NF (175 mV dec^{-1}), and other catalysts with different Ni/Cu ratios (Fig. S2b): Ni_2P (94 mV dec^{-1}), Cu_3P (97 mV dec^{-1}), $\text{Ni}_{1.6}\text{Cu}_{0.4}\text{-P/NF}$ (74 mV dec^{-1}) and $\text{Ni}_{1.4}\text{Cu}_{0.6}\text{-P/NF}$ (86 mV dec^{-1}), respectively. The small Tafel slope of $\text{Ni}_{1.8}\text{Cu}_{0.2}\text{-P/NF}$ demonstrates a high electrocatalytic activity at a low current density [62]. Noticeably, the Tafel slopes of the resulting catalysts are in the range of $40\text{--}120 \text{ mV dec}^{-1}$, indicating that the HER processes in alkaline electrolyte follow the Volmer-Heyrovsky mechanism [42].

Importantly, we also investigated the effect of electrolyzer pH-value on the HER performance of $\text{Ni}_{1.8}\text{Cu}_{0.2}\text{-P/NF}$. As shown in Fig. S2c, the

$\text{Ni}_{1.8}\text{Cu}_{0.2}\text{-P/NF}$ also exhibits a high transfer rate of ions generated in the neutral electrolyte (pH 7), and the overpotential of $\text{Ni}_{1.8}\text{Cu}_{0.2}\text{-P/NF}$ is about 284 mV for sustaining a current density of 10 mA cm^{-2} . With the same testing conditions, the overpotential of $\text{Ni}_{1.8}\text{Cu}_{0.2}\text{-P/NF}$ is only 190 mV in an alkaline media with a pH value of 10. The phenomenon indicates that the electrocatalytic activity of $\text{Ni}_{1.8}\text{Cu}_{0.2}\text{-P/NF}$ is closely related with the OH^- concentration in electrolyte. Normally, the operational stability is also another important performance criterion for the HER process. Fig. 5c demonstrates the potential curves (V-t) of the $\text{Ni}_{1.8}\text{Cu}_{0.2}\text{-P/NF}$ stimulated with a constant current density of 10 mA cm^{-2} , and the generated voltage indicates a successful ultrastable long-term test during the 30 h electrolysis. Moreover, the long-term durability of $\text{Ni}_{1.8}\text{Cu}_{0.2}\text{-P/NF}$ during the HER process was also confirmed by the similar current density and onset potential before and after 10^4 CV cycles (Fig. 5d). The excellent stability of the $\text{Ni}_{1.8}\text{Cu}_{0.2}\text{-P/NF}$

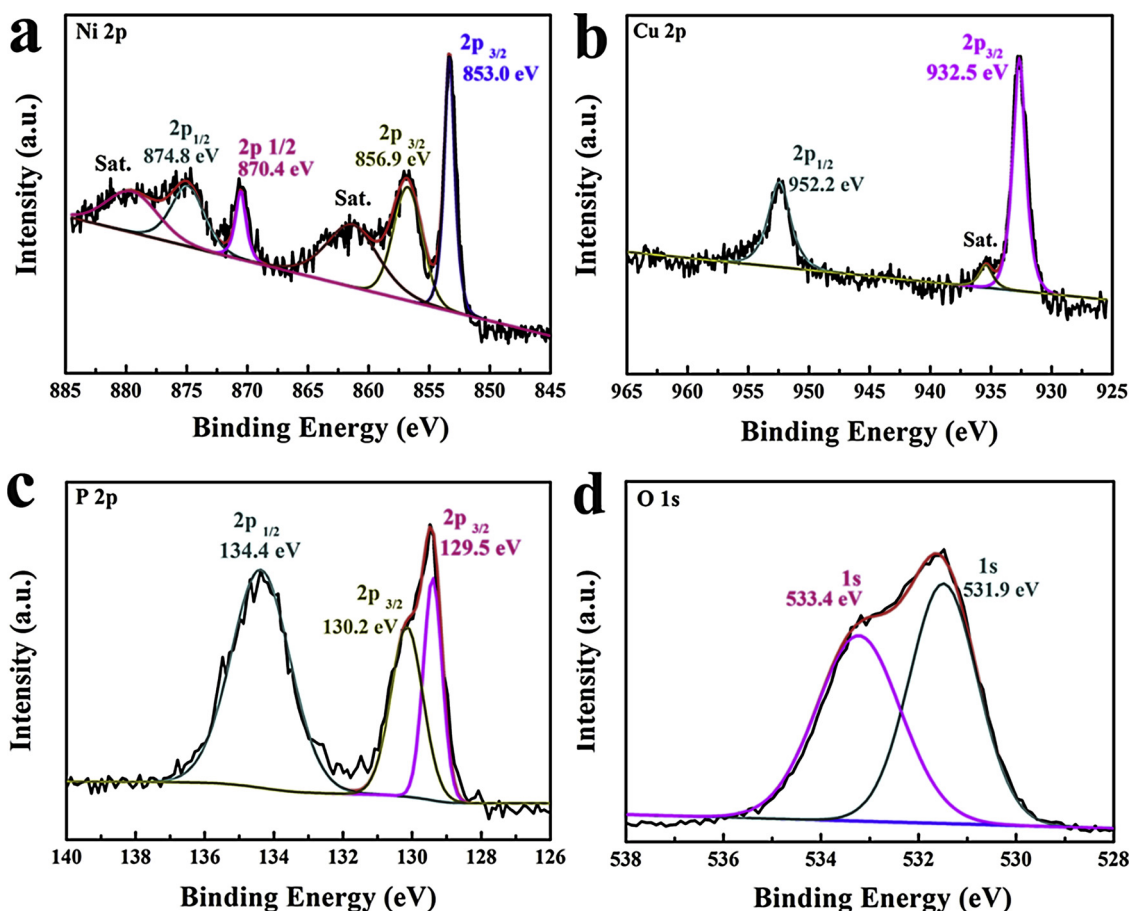


Fig. 4. XPS spectra of $\text{Ni}_{1.8}\text{Cu}_{0.2}\text{-P/NF}$. Peak fitting of (a) Ni 2p, (b) Cu 2p, (c) O 1s, and (d) P 2p narrow-scan spectra.

catalyst after a long-term HER is also proven by the facts established in our experiments: (1) The overall morphology of $\text{Ni}_{1.8}\text{Cu}_{0.2}\text{-P/NF}$ does not significantly change (SEM images: Fig. S3; TEM: Fig. S4); (2) The major phase remains $\text{Ni}_{1.8}\text{Cu}_{0.2}\text{-P}$ as confirmed by the analyses of XPS (Fig. S5), XRD (Fig. S6) and Raman (Fig. S7) spectra.

In order to understand the HER reaction kinetics, the electrochemical impedance spectroscopy (EIS) measurements of different samples were performed. As shown in Fig. 5e, the semicircle in the Nyquist plot of $\text{Ni}_{1.8}\text{Cu}_{0.2}\text{-P/NF}$ exhibits a smaller contact resistance (R_{ct}) than other catalysts, indicating an enhanced electron exchange on the holey $\text{Ni}_{1.8}\text{Cu}_{0.2}\text{-P/NF}$ nanosheet. The measured EIS values of $\text{Ni}_{1.8}\text{Cu}_{0.2}\text{-P/NF}$, NiCu LDH/NF and NF are 1.9, 2.9, and 21.5 Ω , respectively. The smaller R_{ct} of $\text{Ni}_{1.8}\text{Cu}_{0.2}\text{-P/NF}$ may be attributed to the intrinsic metallic characteristic achieved through the continuous network of Ni-Cu or Ni-Ni bonds over all $\text{Ni}_{1.8}\text{Cu}_{0.2}\text{-P/NF}$ layer. Normally, the reduced overpotential and Tafel slope of the catalysts are considered as an important criterion for estimating their electrocatalytic activity.

In addition, the H_2 amount generated with a fixed current density also serves as an important indicator in energy-related applications. With this consideration, the H_2 amount evolved by the $\text{Ni}_{1.8}\text{Cu}_{0.2}\text{-P/NF}$ was explored, and compared with the newly reported advanced catalysts based on non-precious metals. The hydrogen production rate of $\text{Ni}_{1.8}\text{Cu}_{0.2}\text{-P/NF}$ powered at a normalized current density of 10 mA cm^{-2} in 1.0 M KOH is about 1.91 mmol h^{-1} , which is larger than other fabricated catalysts with different Ni/Cu ratio (Fig. 5f and Fig. S2d). Moreover, this value is far larger than those followed state-of-the-art catalysts: $\text{CoS/Ni}_3\text{S}_2\text{-FeS/PNFF}$ (0.68 mmol h^{-1}) [51], $\text{FePSe}_3/\text{rGo}$ (0.356 mmol h^{-1}) [63], $\text{Co}_{0.13}\text{Ni}_{0.87}\text{Se}_2/\text{Ti}$ (0.32 mmol h^{-1}) [11], and Cu/NiFe LDH (0.23 mmol h^{-1}) [56]. We emphasize that the achieved value

is comparable to that generated using commercial Pt/C catalyst (2.8 mmol h^{-1}), and on the other hand, more than 190 times larger than that of $\text{Ni}_x\text{Co}_{3-x}\text{S}_4/\text{Ni}_3\text{S}_2$ (10 $\mu\text{mol h}^{-1}$) [64].

3.3. Understanding $\text{Ni}_{1.8}\text{Cu}_{0.2}\text{-P}$ with DFT Simulations

For further assessment of the influence of Cu atoms on the electrocatalytic performance, we performed the density functional theory (DFT) calculations (Vienna *ab initio* Simulation Package, VASP), which were based on the Ni_2P and $\text{Ni}_{1.8}\text{Cu}_{0.2}\text{-P}$ structures (see Fig. 6a). It should be noted that the energy of Cu doped on the Ni_2P surface is lower than the energy of Cu inserted into the bulk of Ni_2P lattice (Fig. S8a). We thus assume that the Cu doping occurs on the surface of Ni_2P lattice. As shown in Fig. S8b, the Fermi levels of $\text{Ni}_{1.8}\text{Cu}_{0.2}\text{-P}$, Ni_2P and Cu_3P traverse the conduction band without band gap, indicating their metallic characteristics [54], which would certainly facilitate electron transfer during the catalytic reaction. More importantly, the Cu doping helps tune the electronic structure of the original Ni_2P , and provides additional electrons in the valence band and near Fermi surface of $\text{Ni}_{1.8}\text{Cu}_{0.2}\text{-P}$ (see the arrows in Fig. 6b). Compared to the density of states (DOS) for Ni_2P (blue line of Fig. 6b), the main peak near the Fermi level ($-0.4 \sim 0$ eV) in $\text{Ni}_{1.8}\text{Cu}_{0.2}\text{-P}$ (red line of Fig. 6b) shifts to a lower energy level, resulting in the extra electrons provided by Cu-3d that help raise the Fermi level up to a higher energy level. The hybridized states of Cu-3d and P-2p orbitals serve on the respective conductive “wires”, which result in the increase of the coupling effect of the neighboring Ni-P covalent pairs [65].

It is well known that the Gibbs free energy ($\Delta G\text{H}^*$), which is calculated by the equation of $\Delta G(\text{H}^*) = \Delta \text{H}_2(\text{H}^*) + \Delta \text{ZPE} - T\Delta \text{S}$ [66], is an important parameter to indicate the HER activity of electrocatalysts.

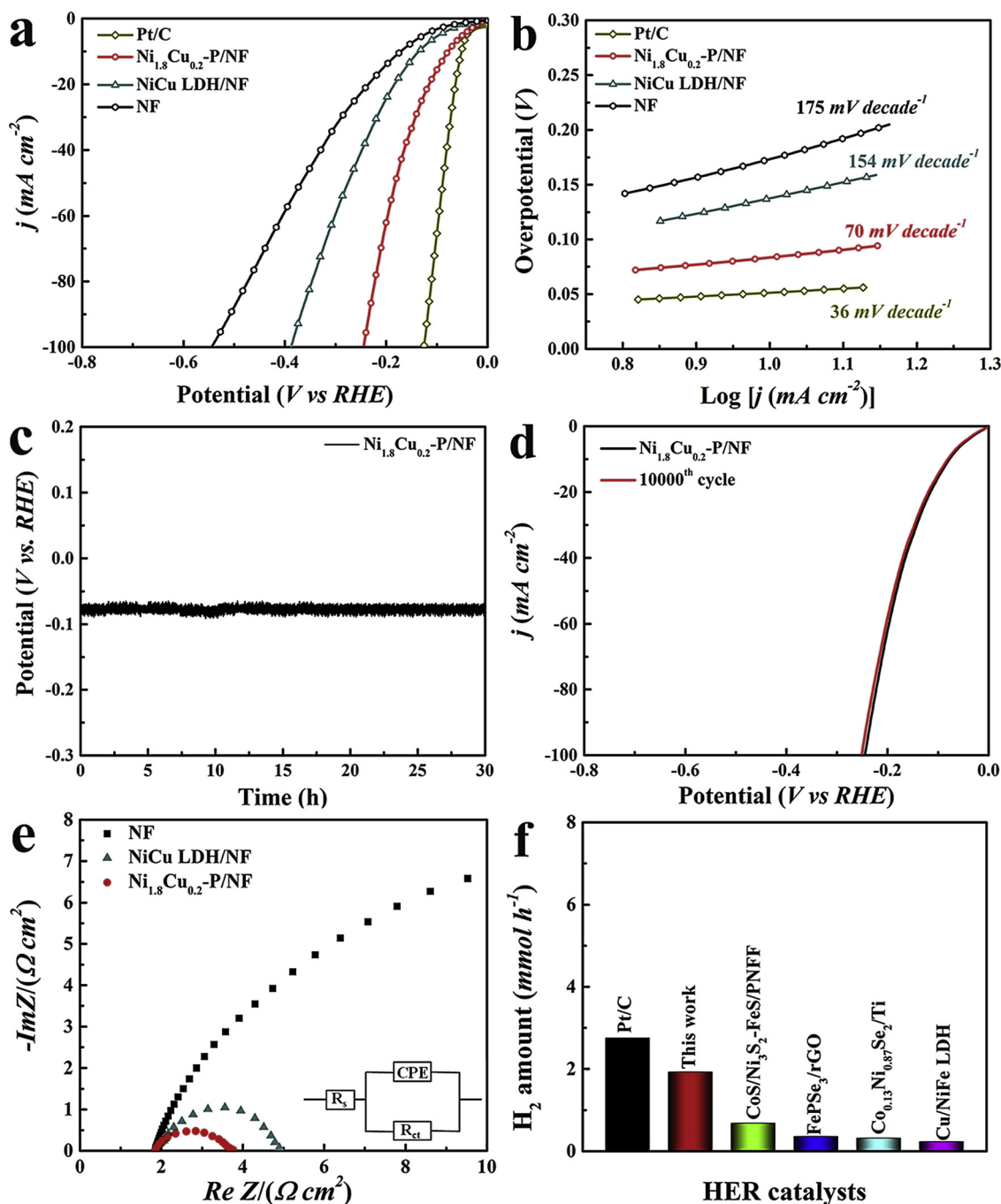


Fig. 5. HER characteristics of different catalysts in 1.0 M KOH. (a) Polarization curves of HER, (b) Corresponding Tafel plots derived from the polarization curves. (c) Time dependent potential profile of $\text{Ni}_{1.8}\text{Cu}_{0.2}\text{-P/NF}$ pushed with a current density of 10 mA cm^{-2} . (d) Polarization curves of $\text{Ni}_{1.8}\text{Cu}_{0.2}\text{-P/NF}$ before and after long-term electrolysis. (e) Nyquist curves for $\text{Ni}_{1.8}\text{Cu}_{0.2}\text{-P/NF}$, NiCu LDH/NF and NF . (f) H_2 gas evolution rate of $\text{Ni}_{1.8}\text{Cu}_{0.2}\text{-P/NF}$ powered by a current density of 10 mA cm^{-2} in comparison with other most advanced non-noble metal catalysts, such as $\text{CoS/Ni}_3\text{S}_2\text{-FeS/PNFF}$ [51], $\text{FePSe}_3/\text{rGO}$ [63], $\text{Co}_{0.13}\text{Ni}_{0.87}\text{Se}_2/\text{Ti}$ [11], and Cu/NiFe LDH [56].

Meanwhile, the value of $\Delta\text{ZPE} - T\Delta\text{S}$ is a constant value for a certain catalytic system [66]. As a result, the $\Delta G(H^*)$ and $\Delta H_2(H^*)$ show a proportional relationship, and the value of $\Delta H_2(H^*)$ can also indicate the HER activity. Therefore, we also calculated the HER free-energy (ΔH_2) changes of Ni_2P (-0.607 eV) and $\text{Ni}_{1.8}\text{Cu}_{0.2}\text{-P}$ (-0.282 eV) in this work (Fig. 6c), and the smaller ΔH_2 of $\text{Ni}_{1.8}\text{Cu}_{0.2}\text{-P}$ indicates that electronic structure engineering by incorporating substitutional Cu decreases the energy barriers for the adsorption of H^+ [67]. The Fermi level and ΔH_2 of Cu doped into the bulk of Ni_2P lattice also changed noticeably (Fig. S8c), indicating that Cu doping indeed can increase the HER performance of Ni_2P nanosheets. Consequently, as suggested by

the electron transfer process sketched in Fig. 6d, substantially less energy Δ ($\Delta < \Delta'$) is required to produce H_2 gas, and the heterostructured $\text{Ni}_{1.8}\text{Cu}_{0.2}\text{-P}$ is more favorable to transfer the current for the HER.

3.4. HER enhancement mechanism

The excellent electrocatalytic activity of the $\text{Ni}_{1.8}\text{Cu}_{0.2}\text{-P}$ for HER process may be attributed to the following factors:

(i) The Cu dopants change the electronic structure and Fermi level of Ni_2P , and further optimize the desorption of hydrogen and reversible adsorption (Fig. 6, and Fig. S8c) [30].

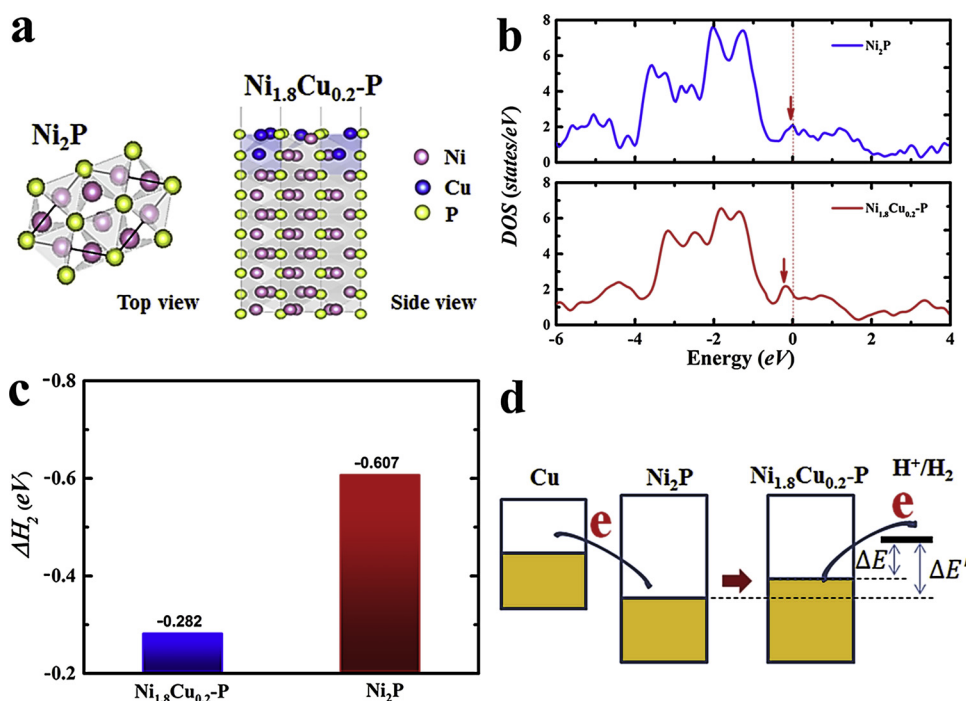


Fig. 6. Theoretical studies of the crystal structures, electronic structure, hydrogen generation and electron transfer properties of $\text{Ni}_{1.8}\text{Cu}_{0.2}\text{-P}$ and Ni_2P . (a) Crystal structures of Ni_2P and $\text{Ni}_{1.8}\text{Cu}_{0.2}\text{-P}$, (b) Calculated DOS for Ni_2P and $\text{Ni}_{1.8}\text{Cu}_{0.2}\text{-P}$, (c) HER free-energy change of Ni_2P doped with Cu, (d) The schematic energy level of Cu atoms in $2\text{H-Ni}_2\text{P}$ to form $\text{Ni}_{1.8}\text{Cu}_{0.2}\text{-P}$ and the charge transfer for HER process.

(ii) As shown in Fig. S9, the holey $\text{Ni}_{1.8}\text{Cu}_{0.2}\text{-P}$ nanosheets dramatically improve the contact area between the catalyst and electrolyte, thus promoting the electron and ion diffusion confirmed through the calculated C_{dl} of $\text{Ni}_{1.8}\text{Cu}_{0.2}\text{-P}$ (31.2 mF cm^{-2}), which is larger than the NiCu LDH/NF (28.4 mF cm^{-2}) and NF (17.6 mF cm^{-2}).

(iii) The metallic nature of the $\text{Ni}_{1.8}\text{Cu}_{0.2}\text{-P}$ clearly decreases the Faradaic impedance, and the electrons from the catalyst electrode are readily collected at the catalytic active sites on each nanosheet [50]. Apart from the HER, the low resistance of $\text{Ni}_{1.8}\text{Cu}_{0.2}\text{-P}$ is also very useful for increasing the oxygen evolution reaction (OER) performance (Fig. S10).

(iv) The nanopores formed on the $\text{Ni}_{1.8}\text{Cu}_{0.2}\text{-P}$ nanosheets generate many active sites, which is indicated by the N_2 adsorption-desorption isotherm (Fig. S11), resulting in the enhanced catalytic performance per geometric area [56]. Meanwhile, the holey structure of $\text{Ni}_{1.8}\text{Cu}_{0.2}\text{-P}$ enables better contact with electrolyte, and promotes the gas release during HER and OER processes.

4. Conclusions

In conclusion, holey $\text{Ni}_{2-x}\text{Cu}_x\text{-P}$ nanosheets have been successfully prepared on the NF surface by a facile and reproducible method. The optimized 3D-structured $\text{Ni}_{1.8}\text{Cu}_{0.2}\text{-P/NF}$ nanocomposite catalyst, mainly exposing the active crystal plane of (201), shows excellent catalytic performance towards HER in alkaline media. A current density of 10 mA cm^{-2} is obtained with a low overpotential of 78 mV , corresponding to a small Tafel slope of 70 mV dec^{-1} . Even for generating a large current density of 100 mA cm^{-2} with $\text{Ni}_{1.8}\text{Cu}_{0.2}\text{-P/NF}$, the needed overpotential is only 245 mV . Importantly, the H_2 amount produced with a current density of 10 mA cm^{-2} is approximately $1.91 \text{ mmol h}^{-1} \text{ cm}^{-2}$, which is the largest value among the reported noble metal-free catalysts. Moreover, the high electrocatalytic activity of $\text{Ni}_{1.8}\text{Cu}_{0.2}\text{-P/NF}$ is also supported by the first principles theoretical calculations of the DOS and Free energy of H^* adsorption.

Acknowledgements

This work is financially supported by National Natural Science Foundation of China under Grant Nos. 51672249, 11665005,

11505032, 51862001, Zhejiang Natural Science Foundations of China under Grant No. LY16A050002, Natural Science Foundation of Jiangxi Province under Grant Nos. 20171BAB211012, 20171ACB21049, 20161BAB211026, the Program for Innovative Research Team of Zhejiang Sci-Tech University, 521 Talent Project of Zhejiang Sci-Tech University, Science and Technology Project of Jiangxi Provincial Department of Education under Grant Nos. GJJ170823, GJJ150981, GJJ170843, the Bidding Project of Gannan Normal University under Grant No. 15zb05, and K. O. appreciates the Australian Research Council for partial support.

Appendix A. Supplementary data

Supplementary material related to this article can be found, in the online version, at doi:<https://doi.org/10.1016/j.apcatb.2018.10.063>.

References

- [1] M.S. Dresselhaus, I.L. Thomas, *Nature* 414 (2001) 332–337.
- [2] S. Jin, *ACS Energy Lett.* 2 (2017) 1937–1938.
- [3] X. Xu, H. Liang, F. Ming, Z. Qi, Y. Xie, Z. Wang, X. Xu, H. Liang, F. Ming, Z. Qi, *ACS Catalysis* 7 (2017) 6394–6399.
- [4] Q.H. Liang, L.X. Zhong, C.F. Du, Y.B. Luo, Y. Zheng, S.Z. Lia, Q.Y. Yan, *Nano Energy* 47 (2018) 257–265.
- [5] J.Q. Tian, J. Chen, J.Y. Liu, Q.H. Tian, P. Chen, *Nano Energy* 48 (2018) 284–291.
- [6] C.G. Morales-Guio, L. Stern, X. Hu, L. Stern, *Chem. Soc. Rev.* 43 (2014) 6555–6569.
- [7] S. Qu, J. Huang, J. Yu, G. Chen, W. Hu, M. Yin, R. Zhang, S. Chu, C. Li, *ACS Applied Materials & Interfaces* 9 (2017) 29660–29668.
- [8] X.D. Wang, H.Y. Chen, Y.F. Xu, J.F. Liao, B.X. Chen, H.S. Rao, D.B. Kuang, C.Y. Su, *Journal of Materials Chemistry A* 5 (2017) 7191–7199.
- [9] Z. Wu, J. Guo, J. Wang, R. Liu, W. Xiao, C. Xuan, K. Xia, D. Wang, *ACS Applied Materials & Interfaces* 9 (2017) 5288–5294.
- [10] N. Laosiripojana, S. Assabumrungrat, *Journal of Power Sources* 158 (2006) 1348–1357.
- [11] T. Liu, A.M. Asiri, X. Sun, *Nanoscale* 8 (2016) 3911–3915.
- [12] J. Luo, L. Steier, M.K. Son, M. Schreier, M.T. Mayer, M. Grätzel, *Nano Letters* 16 (2016) 1848–1857.
- [13] Y. Guo, Z. Yao, C. Shang, E. Wang, *ACS Applied Materials & Interfaces* 9 (2017) 39312–39317.
- [14] Y. Hou, M. Qiu, G. Nam, M.G. Kim, T. Zhang, K. Liu, X. Zhuang, J. Cho, C. Yuan, X. Feng, *Nano Letters* 17 (2017) 4202–4209.
- [15] Y. Jin, X. Yue, C. Shu, S. Huang, P.K. Shen, *Journal of Materials Chemistry A* 5 (2017) 2508–2513.
- [16] A. Kumar, S. Bhattacharyya, *ACS Applied Materials & Interfaces* 9 (2017) 41906–41915.

- [17] K. Liang, L. Guo, K. Marcus, S.F. Zhang, Z. Yang, D.E. Perea, L. Zhou, Y. Du, Y. Yang, *ACS Catalysis* 7 (2017) 8406–8412.
- [18] G.F. Chen, T.Y. Ma, Z.Q. Liu, N. Li, Y.Z. Su, K. Davey, S.Z. Qiao, *Advanced Functional Materials* 26 (2016) 3314–3323.
- [19] S. Han, S. Liu, R. Wang, X. Liu, L. Bai, Z. He, *ACS Applied Materials & Interfaces* 9 (2017) 17186–17194.
- [20] J. Wu, J. Hu, K. Song, J. Xu, H. Gao, *Journal of Alloys & Compounds* 704 (2017) 1–6.
- [21] Y. Xu, W. Tu, S. Yin, M. Kraft, Q. Zhang, R. Xu, *Dalton Transactions* 46 (2017) 10650–10656.
- [22] X. Xu, Y. Chen, W. Zhou, Z. Zhu, C. Su, M. Liu, Z. Shao, *Advanced Materials* 28 (2016) 6442–6448.
- [23] J. Zhang, T. Wang, D. Pohl, B. Rellinghaus, R. Dong, S. Liu, X. Zhuang, X. Feng, *Angewandte Chemie* 55 (2016) 6702–6707.
- [24] Y.Q. Gong, Z.F. Xu, H.L. Pan, Y. Lin, Z. Yang, J.L. Wang, *Journal of Materials Chemistry A* 6 (2018) 12506–12514.
- [25] Y.Q. Gong, Z.F. Xu, H.L. Pan, Y. Lin, Z. Yang, X.Q. Du, *Journal of Materials Chemistry A* 6 (2018) 5098–5106.
- [26] H. Wang, H.W. Lee, Y. Deng, Z. Lu, P.C. Hsu, Y. Liu, D. Lin, Y. Cui, *Nature Communications* 6 (2016) 7261.
- [27] B. Zhang, C. Xiao, S. Xie, J. Liang, X. Chen, Y. Tang, *Chemistry of Materials* 28 (2016) 6934–6941.
- [28] B. You, N. Jiang, M. Sheng, S. Gul, J. Yano, Y. Sun, *Chemistry of Materials* 27 (2015) 7636–7642.
- [29] S. Dutta, A. Indra, Y. Feng, T. Song, U. Paik, *ACS Applied Materials & Interfaces* 9 (2017) 33766–33774.
- [30] M.D.D. Mello, F.D.A. Braggio, B.D.C. Magalhães, J.L. Zotin, M.A.P.D. Silva, *Industrial & Engineering Chemistry Research* 56 (2017) 6934–6941.
- [31] Y. Yang, K. Zhang, H. Lin, X. Li, H.C. Chan, L. Yang, Q. Gao, *ACS Catalysis* 7 (2017) 2357–2366.
- [32] Z. Wang, H.T. Du, Z.A. Liu, H. Wang, A.M. Asiri, X.P. Sun, *Nanoscale* 10 (2018) 2213–2217.
- [33] Y.Y. Ji, L. Yang, X. Ren, G.W. Cui, X.L. Xiong, X.P. Sun, *ACS Sustainable Chemistry & Engineering* 6 (2018) 11186–11189.
- [34] J.Q. Tian, Q. Liu, N.Y. Cheng, A.M. Asiri, X.P. Sun, *Angewandte Chemie* 53 (2014) 9577–9581.
- [35] H.F. Du, Q. Liu, N.Y. Cheng, A.M. Asiri, X.P. Sun, C.M. Li, *Journal of Materials Chemistry A* 2 (2014) 14812–14816.
- [36] X. Zou, Y. Zhang, *Cheminform* 44 (2015) 5148–5180.
- [37] Y. Lin, L. He, T. Chen, D. Zhou, L. Wu, X. Hou, C. Zheng, *Journal of Materials Chemistry A* 6 (2018) 4088–4094.
- [38] X.-D. Wang, Y. Cao, Y. Teng, H.-Y. Chen, Y.-F. Xu, D.-B. Kuang, *ACS Applied Materials & Interfaces* 9 (2017) 32812–32819.
- [39] C. Guan, H. Wu, W. Xiao, X. Liu, W. Zang, H. Zhang, J. Ding, Y.P. Peng, S.J. Pennycook, J. Wang, *Nano Energy* 48 (2018) 73–80.
- [40] Y. Liu, Y. Zhu, J. Shen, J. Huang, X. Yang, C. Li, *Nanoscale* 10 (2018) 2603–2612.
- [41] R. Zhang, C. Tang, R. Kong, G. Du, A.M. Asiri, L. Chen, X. Sun, *Nanoscale* 9 (2017) 4793–4800.
- [42] C. Du, M. Shang, J. Mao, W. Song, *Journal of Materials Chemistry A* 5 (2017) 15940–15949.
- [43] C. Huang, C. Pi, X. Zhang, K. Ding, P. Qin, J. Fu, X. Peng, B. Gao, P.K. Chu, K. Huo, *Small* 14 (2018) 1800667.
- [44] Y.C. Dong, S.W. Jun, G. Yoon, H. Kim, M.Y. Ji, K.S. Lee, T. Kim, H. Shin, A.K. Sinha, S.G. Kwon, *Journal of the American Chemical Society* 139 (2017) 6669–6674.
- [45] D. Li, Q. Liao, B. Ren, Q. Jin, H. Cui, C. Wang, *Journal of Materials Chemistry A* 5 (2017) 11301–11308.
- [46] W. Cai, W. Liu, J. Han, A. Wang, *Biosensors & Bioelectronics* 80 (2016) 118–122.
- [47] H. Jin, J. Wang, D. Su, Z. Wei, Z. Pang, Y. Wang, *Journal of the American Chemical Society* 137 (2015) 2688–2694.
- [48] W. Ma, R. Ma, C. Wang, J. Liang, X. Liu, K. Zhou, T. Sasaki, *ACS Nano* 9 (2015) 1977–1984.
- [49] A. Sivanantham, P. Ganesan, S. Shanmugam, *Advanced Functional Materials* 26 (2016) 4660–4660.
- [50] A. Han, H. Zhang, R. Yuan, H. Ji, P. Du, *ACS Applied Materials & Interfaces* 9 (2017) 2240–2248.
- [51] S. Qu, W. Chen, J. Yu, G. Chen, R. Zhang, S. Chu, J. Huang, X. Wang, C. Li, K. Ostrikov, *Journal of Power Sources* 390 (2018) 224–233.
- [52] X. Chen, P. Li, Z. Jin, Y. Meng, H. Yuan, D. Xiao, *Journal of Materials Chemistry A* 5 (2017) 18786–18792.
- [53] P. Chen, T. Zhou, M. Zhang, Y. Tong, C. Zhong, N. Zhang, L. Zhang, C. Wu, Y. Xie, *Advanced Materials* 29 (2017) 1701584.
- [54] H. Liang, A.N. Gandi, D.H. Anjum, X. Wang, U. Schwingenschlög, H.N. Alshareef, *Nano letters* 16 (2016) 7718–7725.
- [55] H. Liang, L. Li, F. Meng, L. Dang, J. Zhuo, A. Forticaux, Z. Wang, S. Jin, *Chemistry of Materials* 27 (2015) 5702–5711.
- [56] L. Yu, H. Zhou, J. Sun, F. Qin, F. Yu, J. Bao, Y. Yu, S. Chen, Z. Ren, *Energy & Environmental Science* 10 (2017) 1820–1827.
- [57] P. Luo, H. Zhang, L. Liu, Y. Zhang, J. Deng, C. Xu, N. Hu, Y. Wang, *ACS Applied Materials & Interfaces* 9 (2017) 2500–2508.
- [58] K. Xu, H. Ding, K. Jia, X. Lu, P. Chen, T. Zhou, H. Cheng, S. Liu, C. Wu, Y. Xie, *Angew Chem Int Ed* 55 (2016) 1710–1713.
- [59] L. Zeng, K. Sun, Z. Yang, S. Xie, Y. Chen, Z. Liu, Y. Liu, J. Zhao, Y. Liu, C. Liu, *Journal of Materials Chemistry A* 6 (2018) 4485–4493.
- [60] Z. Xiao, Y. Wang, Y.-C. Huang, Z. Wei, C.-L. Dong, J. Ma, S. Shen, Y. Li, S. Wang, *Energy & Environmental Science* 10 (2017) 2563–2569.
- [61] M. Li, T. Liu, X. Bo, M. Zhou, L. Guo, *Journal of Materials Chemistry A* 5 (2017) 5413–5425.
- [62] H. Zhu, L. Gu, D. Yu, Y. Sun, M. Wan, M. Zhang, L. Wang, L. Wang, W. Wu, J. Yao, *Energy & Environmental Science* 10 (2016) 321–330.
- [63] D. Mukherjee, P.M. Austeria, S. Sampath, *ACS Energy Letters* 1 (2016) 367–372.
- [64] Y. Wu, Y. Liu, G.D. Li, X. Zou, X. Lian, D. Wang, L. Sun, T. Asefa, X. Zou, *Nano Energy* 35 (2017) 161–170.
- [65] D. Wang, X. Wang, Y. Lu, C. Song, J. Pan, C. Li, M. Sui, W. Zhao, F.Q. Huang, *Journal of Materials Chemistry A* 5 (2017) 22618–22624.
- [66] L.L. Feng, G.T. Yu, Y.Y. Wu, G.D. Li, H. Li, Y.H. Sun, T.S. Asefa, W. Chen, X.X. Zou, *Journal of the American Chemical Society* 137 (2015) 14023–14026.
- [67] B. Liu, Y.F. Zhao, H.Q. Peng, Z.Y. Zhang, C.K. Sit, M.F. Yuen, T.R. Zhang, C.S. Lee, W.J. Zhang, *Advanced Materials* 29 (2017) 1606521.